Chapter 5

A robust bifunctional $Co_3O_4/Co_xCe_{1-x}O_{2-\delta}/C$ electrocatalyst with crystalline-amorphous interfaces toward ORR and OER

Outline

In this work, we report a robust cobalt and ceria-based catalyst, viz. $Co_3O_4/Co_xCe_{1-x}O_{2-\delta}/C$ that is high performing, stable and bifunctional. This work is yet another testament to the predicament that CeO_2 imparts beneficial modifications to Co_3O_4 [1,2]. Co_3O_4 has a high specific capacitance and great redox properties [3]. Cerium, on the other hand, is an abundantly found lanthanoid which exhibits unique properties like tunable Ce^{3+}/Ce^{4+} content, high oxygen affinity and anti-corrosive nature [4]. It is often exploited as a special support for electrocatalysts. Hence, nano-engineering a low-cost, non-noble metal-based active element like $M^1M^2O_{x-y}$ (where M^1=Co, M^2=Ce) with intricately designed CeO_2 is an emerging technique in catalyst design [5]. Although there are multiple reports of such CeO_2-based transition metal catalysts, our method is a relatively simpler one-pot technique and utilizes non-toxic metal precursors. Unlike that in Chapter 4, we employ a mild calcination in this study to impart beneficial alterations to the crystallinity of Co_3O_4 and CeO_2. The calcination dopes some amount of Co^{2+} and Co^{3+} ions into the CeO_2 lattice. This is attributed to give an additional boost to the overall catalyst performances by generating important point defects [3]. Like the other chapters, the catalysts are further improved by incorporating graphene nanoplatelets as the conductivity enhancer. Graphene nanoplatelets, which is a two-dimensional framework of carbon atoms packed in hexagonal network with occasional defects, is evolving as a great additive in electrocatalysts. These are compact few layered graphene sheets with high surface area (typically ~2630 $m^2\ g^{-1}$) and thermal conductivity as high as 5000 W/mK. Both these traits extremely help in charge carrier mobility during the ORR, OER processes [6].

The synthesis procedure of the catalysts $Co_3O_4/Co_xCe_{1-x}O_{2-\delta}/C$, Co_3O_4/C and CeO_2/C are described in Section 2.2.7, 2.2.8 and 2.2.9, respectively. Their physical characterization and electrocatalytic activities have been described below.

5.1 Results and discussion

5.1.1 Physical characterization of the catalysts

The synthesized catalysts were characterized for their physico-chemical properties with standard characterization techniques such as, PXRD, FTIR and Raman spectroscopy, EDX, BET surface area measurement, TGA, TEM and XPS.

The crystallinity and phase identification of the catalysts is done through their PXRD spectra shown in Figure 5.1. A peak at $2\theta = 26.5°$ is observed in all three which represents the (002) plane of graphene nanoplatelets. The generated spectra resonate well with JCPDS card nos. 65-3103 and 81-0792 depicting formation of Co_3O_4 and CeO_2 respectively. All diffraction peaks are indexed to their respective Miller indices. The hybrid catalyst $Co_3O_4/Co_xCe_{1-x}O_{2-\delta}/C$ exhibits diffraction peaks from both Co_3O_4 and CeO_2. However, for $Co_3O_4/Co_xCe_{1-x}O_{2-\delta}/C$, the peaks occurring at $2\theta = 59.5°, 70.1°, 77.4°$ representing planes (222), (400), (331) arising from CeO_2 has a shift by +0.5°, +0.6° and +0.8°, respectively. This signifies compressive strain in CeO_2 crystallites most plausibly due to doping of $Co^{2+/3+}$ ions into CeO_2 lattice which results in lowering in interplanar distances (d) [7]. Peak broadening and Bragg shift in $Co_3O_4/Co_xCe_{1-x}O_{2-\delta}/C$ indicate inhomogeneously strained crystallites. This could also arise from lattice defects like doping, interstitials, vacancies and dislocations. Closely packed grain boundaries are attributed to aid in generating inhomogeneous layer strains and therefore the inhomogeneous Bragg diffractions [8]. Decrease in peak intensity and peak broadening is also observed for $Co_3O_4/Co_xCe_{1-x}O_{2-\delta}/C$ which clearly indicates decrease in phase crystallinity. Moreover, (311) plane of Co_3O_4 dominates in the hybrid catalyst $Co_3O_4/Co_xCe_{1-x}O_{2-\delta}/C$ instead of (220) and (222) as was observed for $Co_3O_4/Co_xCe_{1-x}O_{2-\delta}$. (311) of Co_3O_4 is responsible for enhanced performance. The average crystallite sizes are determined from the Scherrer equation [9]:

$$D = \frac{K\lambda}{\beta\cos\theta}$$

where D is the crystallite size in nm, K is the shape factor constant in the range 0.8–1.2 (typically equal to 0.9 for spherical shape), λ is the wavelength of radiation, β is the full width half maxima (FWHM) of the diffraction and θ is the Bragg's diffraction angle. The results from Scherrer calculation are tabulated in Table 5.1.

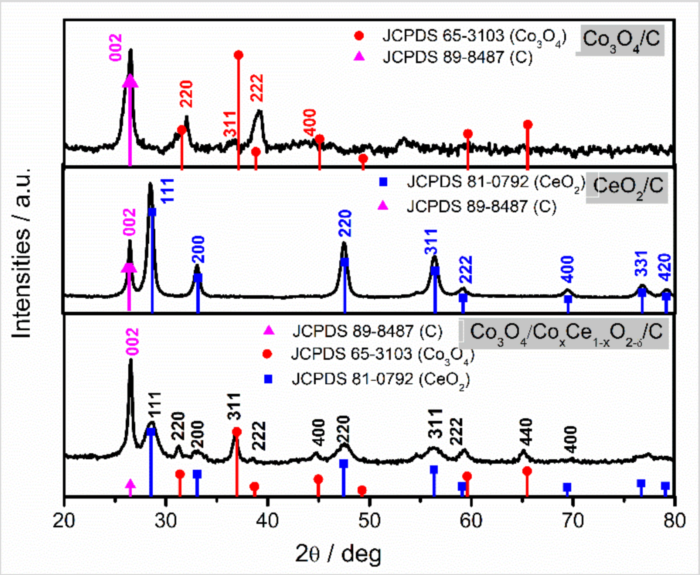

Figure 5.1. PXRD spectra of the as-synthesized catalysts.

Table 5.1. Average crystallite sizes as calculated from Scherrer equation.

Catalyst	Av. Crystallite size (nm)	Av. Crystallite size in $Co_3O_4/Co_xCe_{1-x}O_{2-\delta}/C$ (nm)	Change in crystallite size
Co_3O_4	8.3	42.6	Increase by 5 times
CeO_2	10.9	7.1	Decrease by 0.6 times

It is observed from Table 5.1 that average crystallite size of Co_3O_4 increases 5-folds while that of CeO_2 decrease 0.65-folds. This clearly indicates increase in crystallinity of Co_3O_4 and decrease in crystallinity of CeO_2 in the mixed oxide $Co_3O_4/Co_xCe_{1-x}O_{2-\delta}$ [9]. The decrease in crystallite sizes of CeO_2 in $Co_3O_4/Co_xCe_{1-x}O_{2-\delta}$ can be attributed to the doping of $Co^{2+/3+}$ ions into CeO_2 lattice [7].

Figure 5.2 (a) presents the FTIR spectra of the catalysts in which there is a broad and intense band for −OH group at ~3427 cm^{-1} (arising from surface adsorbed H_2O molecules) [10], two narrow and shar bands for $-CH_2$ at ~2847 cm^{-1} and 2919 cm^{-1} (arising from graphene nanoplatelets framework), less intense bands at ~1740 cm^{-1} for C=O (arising from surface oxidation of graphene carbon), less intense but sharp bands at ~1570 cm^{-1} and 1622 cm^{-1} for C=C (arising from graphene nanoplatelets framework) [11]. The remaining bands in the range 400−1000 cm^{-1} arise from M–O bonds (M= Co, Ce) [10,12]. Figure 5.2 (b) shows the TGA graph of the as-synthesized catalysts in air atmosphere where all the graphene C leaves as CO_2, leaving behind 30 wt.% of the MO_x content. This confirms the correct %mass loading of the active component with the graphene support.

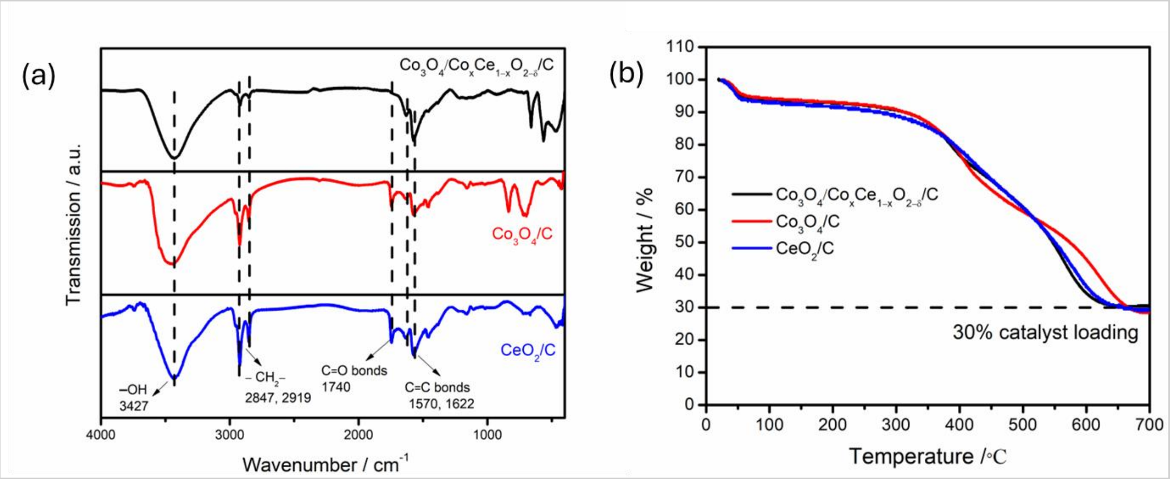

Figure 5.2. (a) FTIR spectra (b)TGA curve in air atmosphere.

The Raman spectra of the catalysts are shown in Figure 5.3. Figure 5.3 (a) shows the D-band (I_D) at ~1344 arising from sp^3 defects in the crystal lattice and a G-band (I_G) band at ~1575 cm^{-1} arising E_{2g} phonons of sp^2 carbon atoms in the graphene nanoplatelets. Another band depicted as 2D band is observable at ~2700 cm^{-1} which is a typical observation for graphene. A narrow 2D band depicts lower degree of disorderliness [13]. Other observable Raman active vibrational modes viz. CeO_2 (F_{2g}) [5,7] and Co_3O_4 (E_g, F_{2g}, A_{1g}) [5,9,12,14] are shown in Figure 5.3 (b). It is to be noted that for $Co_3O_4/Co_xCe_{1-x}O_{2-\delta}$, there is a negative shift (red shift) of ~8.4 cm^{-1} for F_{2g} (CeO_2) which indicates decrease in crystallite sizes [9] (which corroborates well with the findings from

Scherrer calculation from PXRD). It is also representative of more oxygen vacancies in the mix oxide than in CeO_2 and is presumed to occur due to the thermal treatment. Raman spectroscopy is very sensitive to sub-surface oxygen environment and point defects (oxygen vacancies) [15]. Substantial decrease in the intensity of A_{1g} and F_{2g} in $Co_3O_4/Co_xCe_{1-x}O_{2-\delta}$ and peak broadening indicates decrease in crystallinity in the mixed metal oxide [7] which is again due to the thermal treatment.

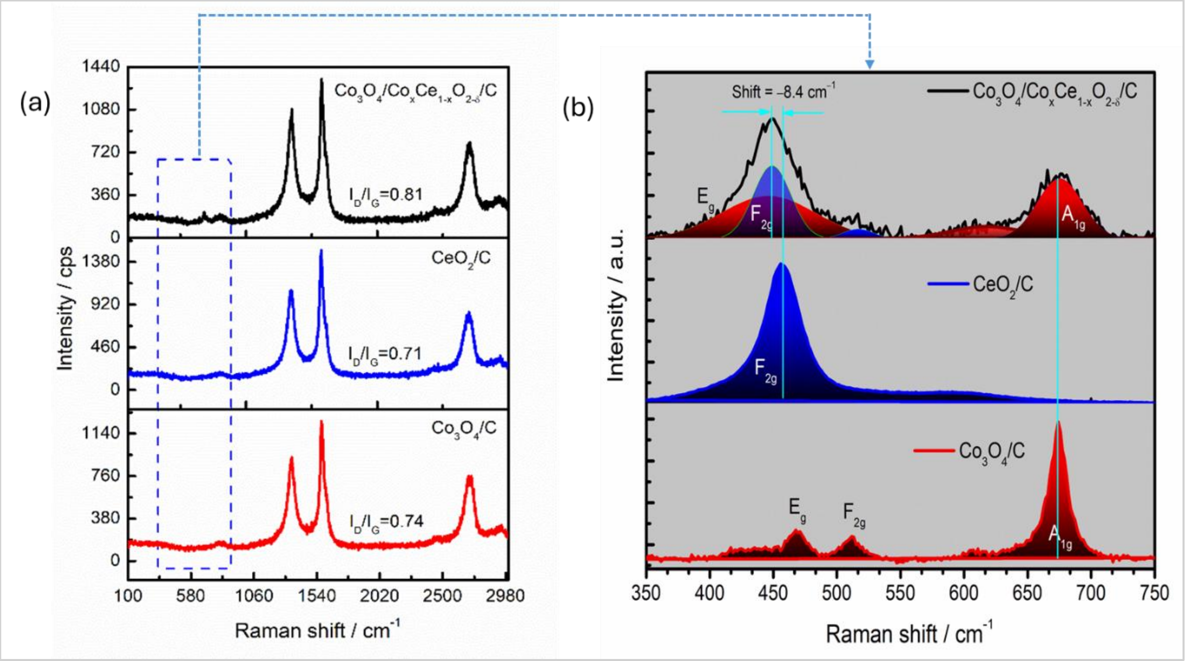

Figure 5.3. (a) Raman spectra showing I_D/I_G values, and (b) Raman spectra showing vibrational modes and shifts in F_{2g} peak in $Co_3O_4/Co_xCe_{1-x}O_{2-\delta}/C$.

The morphology of the $Co_3O_4/Co_xCe_{1-x}O_{2-\delta}/C$ is observed under a high-resolution electron microscope to get more insights into the morphology and crystal defects.

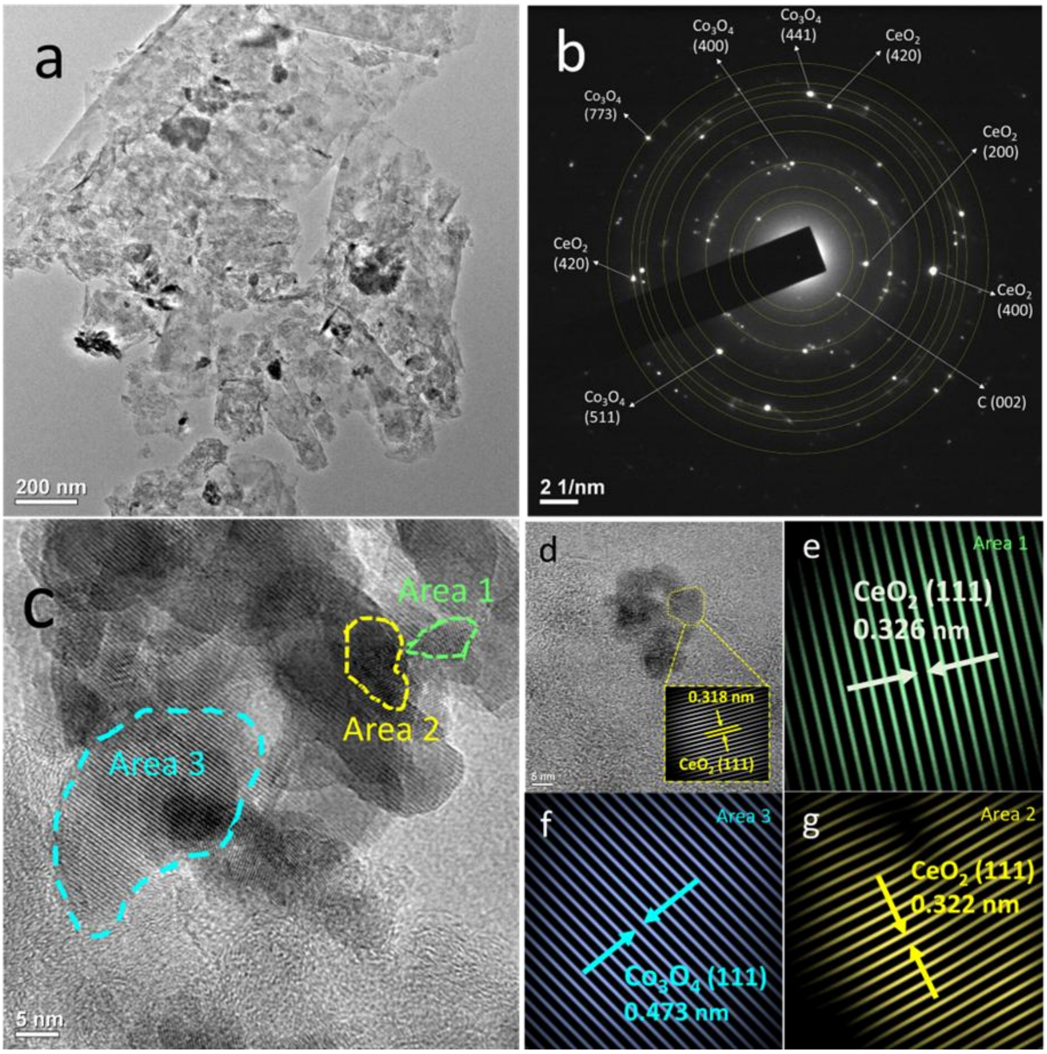

Figure 5.4. (a) TEM images of $Co_3O_4/Co_xCe_{1-x}O_{2-\delta}/C$ (b) SAED pattern with rings indexed to appropriate Miller planes (c,d) HR-TEM images showing lattice fringes and interplanar spacing (e-g) inverse FFTs of depicted areas in (c).

These images are presented in Figure 5.4. Figure 5.4 (a) shows that $Co_3O_4/Co_xCe_{1-x}O_{2-\delta}/C$ agglomerates are embedded on the encrusted graphene surfaces. It is assumed that there exists a strong adherence of the agglomerates on to the carbon support as they do not escape the periphery of the graphene sheets. This should render good conductivity in the electrocatalysis process. Figure 5.4 (b) shows the SAED pattern with multiple dotted and overlapping concentric rings depicting the polycrystalline nature of the material. Figure 5.4 (c-d) are HR-TEM images that shows various crystallites and different observable lattice fringes. The inverse First Fourier Transform (FFT) images of these fringes generated from ImageJ software are shown in Figure 5.4 (e-g) with interplanar distances indexed to their appropriate Miller planes (h k l). Concomitant with Scherrer calculations, crystallites of Co_3O_4 are seen to be much larger than those of CeO_2. The HR-TEM images also shows clearly that there is proximity among the different crystallites of Co_3O_4 and CeO_2 rendering to generation of large degrees of inhomogeneity in packing and creation of heterogeneous oxide-oxide interfaces.

The XPS wide range survey spectrum of the catalysts reveal presence of the elements C, O, Co and Ce as presented in Figure 5.5 (a). All XPS peaks have been corrected with respect to the adventitious C 1s peak at 284.6 eV. Figure 5.5 (b) shows that O 1s spectrum exhibits two humps deconvoluted into three peaks represented by O_L for lattice oxygen (O^{2-}), O_V for oxygen vacancy (electron ejecting from surface atoms with oxygen defects in its co-ordination shell) and O_S for surface oxygen atoms (OH^-,adsorbed H_2O molecules, etc.) [16–18]. O_L is observed at ~530 eV, O_V at ~531 eV and O_S at ~532 eV. It is to be noted that there is a shift in O_L in Co_3O_4/C towards higher B.E. which could be possibly due to presence of higher amount of Co^{3+} in Co_3O_4/C (lower value of Co^{2+} / Co^{3+}) than $Co_3O_4/Co_xCe_{1-x}O_{2-\delta}/C$. Quantitative analysis by area integration of deconvoluted peaks shows that O_L/O_S ratio is the highest for $Co_3O_4/Co_xCe_{1-x}O_{2-\delta}/C$ (6.7), followed by CeO_2/C (3.9) and then by Co_3O_4/C (3.1). This indicates that $Co_3O_4/Co_xCe_{1-x}O_{2-\delta}/C$ has excessive amount of surface-adsorbed oxygen species [17] which arises from excessive oxygen defects. Under normal conditions, these defects are satisfied by weakly adsorbed functional groups like H_2O and OH^-. Figure 5.5 (b) shows that O_v is the least for Co_3O_4/C (~ 0%), followed by CeO_2/C (2.5%) and the highest in $Co_3O_4/Co_xCe_{1-x}O_{2-\delta}/C$ (3.5%). This is the benefit of combining Co_3O_4/C with CeO_2. These oxygen defects are presumed to arise from CeO_2/C and are expected to act as active sites for ORR performance [5].

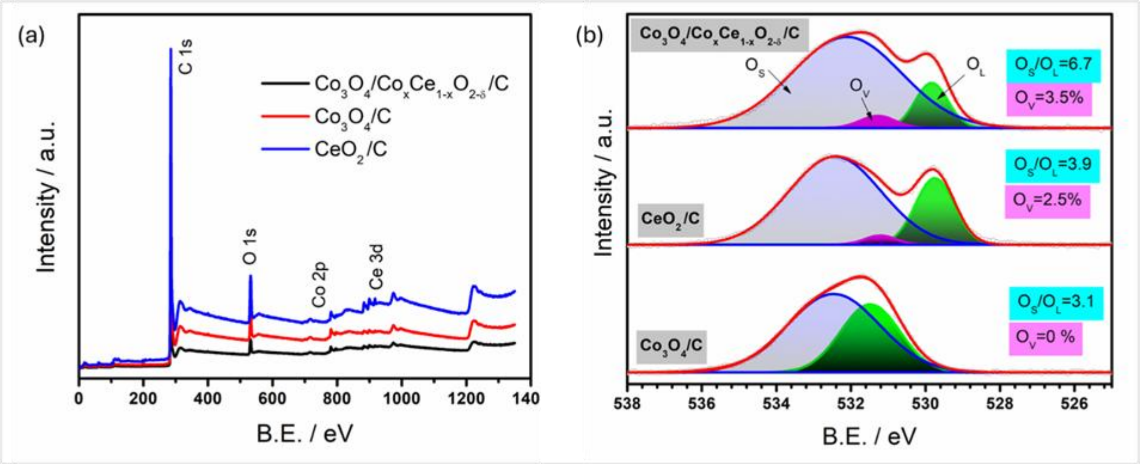

Figure 5.5. (a) XPS survey spectra, and (b) O 1s core XP spectra with O_S/O_L ratios and %composition of O_V mentioned of the as-synthesized catalysts.

To correlate the surface oxygen vacancy concentration, the Co 2p XPS measurement is performed. As seen from Figure 5.6, the Co 2p spectra comprises of two satellite peaks (~785 eV and ~803 eV) and two major peaks depicting $2p_{1/2}$ and $2p_{3/2}$ spin states observed at ~781 eV and ~797 eV respectively [10,12,18–20]. The shifts in binding energies for Co 2p XPS spectra are presented in Table 5.2. The binding energies are shifted to a lower energy in the mix oxide. Quantitative analysis was done by integrating peak areas of deconvoluted XPS spectra. The amount of Co^{2+} : Co^{3+} determined by quantitative analysis is 3.6 for the mix oxide and 0.8 for Co_3O_4/C. This is an important parameter [10] which indicates that the content of Co^{2+} is higher in the mix oxide which makes the Co 2p photoemission easier and hence correlates to the lower binding energies in $Co_3O_4/Co_xCe_{1-x}O_{2-\delta}/C$. The lowering of Co^{2+} ions in the mix oxide also indicates that there are lesser O^{2-} in the bulk of $Co_3O_4/Co_xCe_{1-x}O_{2-\delta}/C$. this is a clear indicative of oxygen defects in the mix oxide which does not happen in Co_3O_4/C.

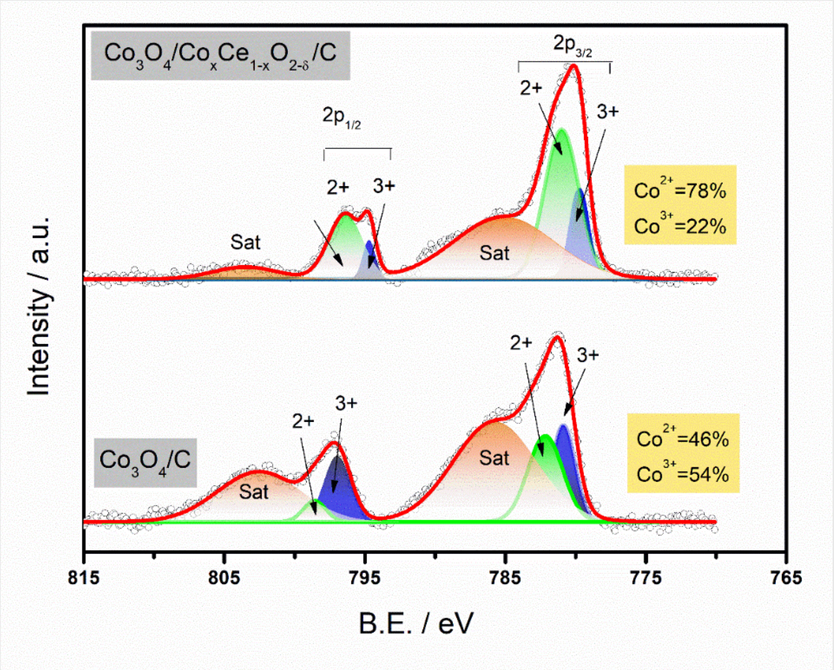

Figure 5.6. Co 2p core XP spectra of $Co_3O_4/Co_xCe_{1-x}O_{2-\delta}/C$, Co_3O_4/C and CeO_2/C.

Table 5.2. Shifts in binding energies (B.E.) of Co 2p XPS spectra.

Species	BE (eV) in Co_3O_4/C	BE (eV) in $Co_3O_4/Co_xCe_{1-x}O_{2-\delta}/C$	Shifts in BE (eV)
Co^{3+}	780.8	779.7	1.1
Co^{2+}	782.1	780.9	0.6
Co^{3+}	796.9	794.6	2.2
Co^{2+}	798.5	796.3	2.2

Again, Figure 5.7 shows the XP spectra of core Ce 3d. The spectra are deconvoluted into 8 peaks, two of which (marked as u′ and v′) arise from Ce^{3+} [21,22]. No difference was observed for core Ce 3d XP spectra of $Co_3O_4/Co_xCe_{1-x}O_{2-\delta}/C$ and CeO_2/C. This could be due to ‘x’ being very low quantity at the surface to be detectable by the X-rays. However, the intensity of the peaks is lower for the mix oxide, indicating that there are lower of total $Ce^{3+/4+}$ content in $Co_3O_4/Co_xCe_{1-x}O_{2-\delta}/C$ due to Co-doping in CeO_2.

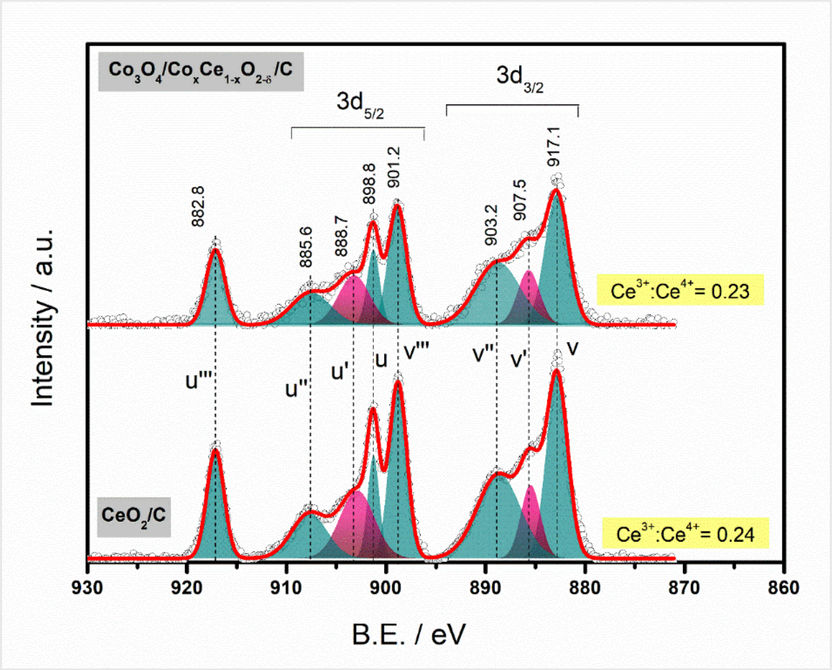

Figure 5.7. Ce 3d core XP spectra of $Co_3O_4/Co_xCe_{1-x}O_{2-\delta}$/C and CeO_2/C.

5.1.2 Electrocatalytic study

The catalysts were tested for their electrochemical activities for ORR and OER with a Metrohm Autolab PGSTAT 204 (Netherlands) workstation comprising of a standard 3-electrode system. A 3 mm glassy-carbon rotating disk electrode (GC-RDE) as working electrode, a 20 × 10 mesh of Pt as counter electrode and a single-junction Hg/HgO in 0.1 M KOH as the reference electrode are employed in 0.1 M is KOH as the supporting electrolyte. The working electrode ink was made from 5 mg catalyst mixed with 1:1 water-isopropanol mixture and sonicated for 30 min. After that, 500 µL of 0.5% Nafion solution is added and sonicated for another 30 min to obtain a homogeneous ink. From this, 3 µL is drop casted on to the glassy carbon electrode for electrochemical measurements.

The electrocatalytic activity of the as-synthesized catalysts toward ORR/OER is studied in 0.1M KOH (pH=13) solution which is a common electrolyte in alkaline fuel cells. Figure 5.8 demonstrates their well-defined ORR polarization curves.

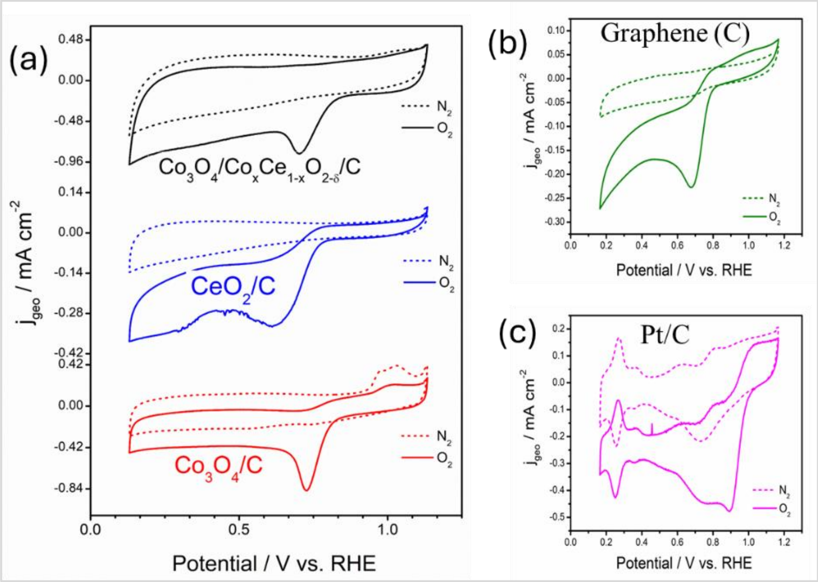

Figure 5.8. CVs of (a) as-synthesized catalysts, (b) graphene nanoplatelets, and (c) commercial 20 wt% Pt/C, in N_2- and O_2-saturated 0.1M KOH at scan rate 10 mV s^{-1}.

The LSVs of all the studied catalysts are carried out at five different rotation rates in the range 400–3600 rpm (shown in Figure 5.9).

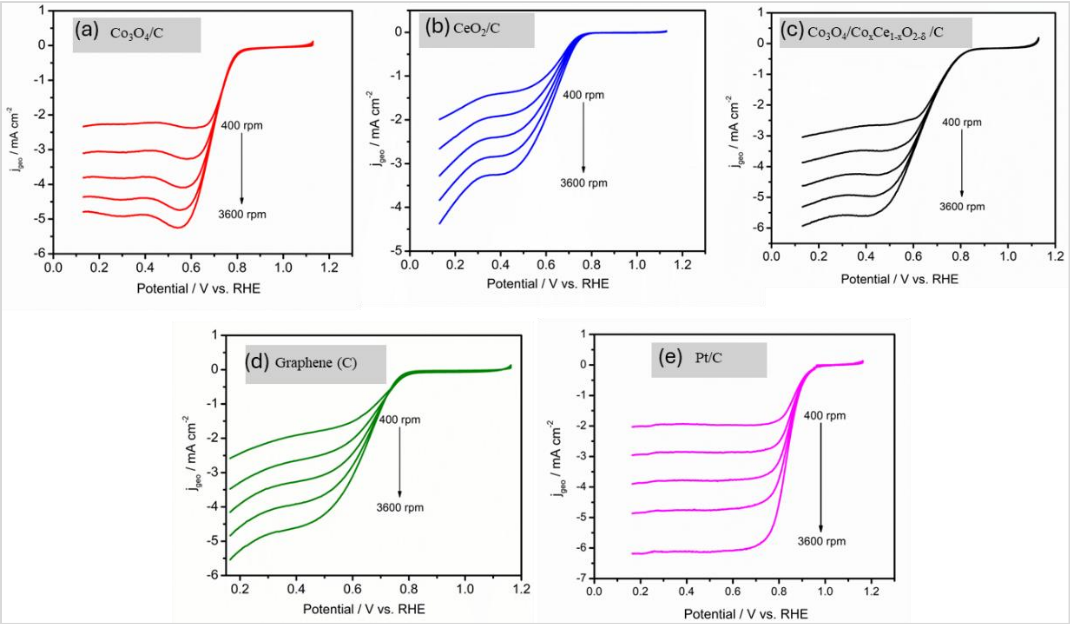

Figure 5.9. LSVs of (a–c) the as-synthesized catalysts, (d) of graphene nanoplatelets (C), and (e) of commercial 20 wt.% Pt/C, in O_2-saturated 0.1M KOH at scan rate 10 mV s^{-1}.

Table 5.3. Evaluated electrocatalytic parameters of the as-synthesized catalysts and the benchmark Pt/C and RuO_2.

Catalysts	$E_{onset,ORR}$ / V	TOF / s^{-1}	$E_{1/2}$ / V	η_{10} / mV	j_{geo} / $mAcm^{-2}$	ECSA / m^2g^{-1}
$Co_3O_4/Co_xCe_{1-x}O_{2-\delta}/C$	0.85 V	0.259	0.67	500	−4.26	810
Co_3O_4/C	0.85 V	0.032	0.72	710	−3.80	760
CeO_2/C	0.77 V	0.023	0.61	870	−2.40	170
Pt/C	0.98 V	–	0.84		−3.80	–
RuO_2	–	0.025	–	500	–	–

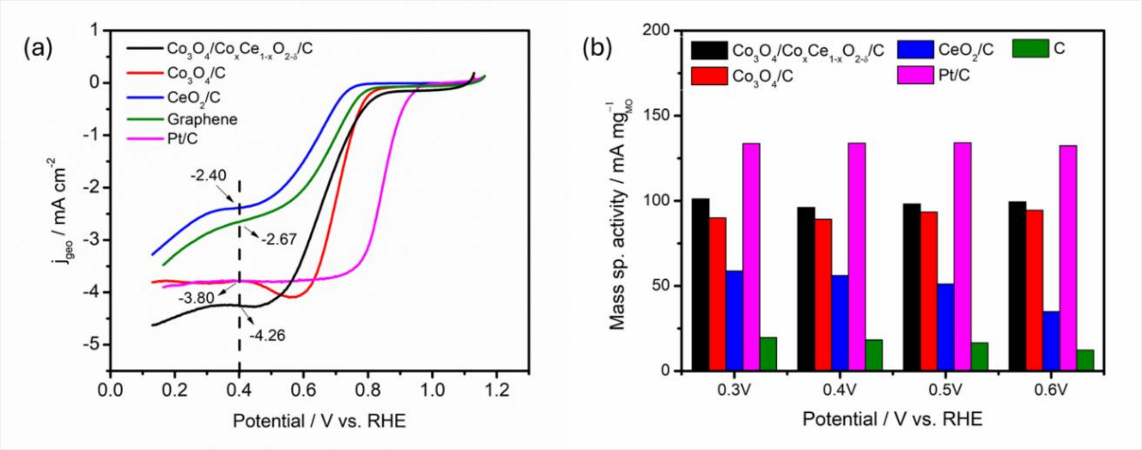

Figure 5.10. (a) A comparative overlay of LSV@1600 rpm of the studied catalysts in O_2-saturated 0.1M KOH; scan rate 10 mVs^{-1}, and (b) Bar diagram of mass specific activities of the catalysts calculated at 0.4 V.

While $E_{onset,ORR}$ for both $Co_3O_4/Co_xCe_{1-x}O_{2-\delta}/C$ and Co_3O_4/C is 0.85V, the half-wave potential ($E_{1/2}$) of Co_3O_4/C is seen to be the earliest (0.74 V) among the three as-synthesized catalysts. The LSVs at 1600 rpm of the as-synthesized catalysts have been overlayed upon those of graphene nanoplatelets (C) and 20 wt% Pt/C (commercial standard for ORR). This is presented in Figure 5.10 (a). In terms of geometric current density (j_{geo}) at a potential 0.4 V, the mix oxide-oxide catalyst $Co_3O_4/Co_xCe_{1-x}O_{2-\delta}/C$ is superior to its component oxides, indicating the beneficial aspects of mixed oxide interfaces in the mas transport regime. Figure 5.10 (b) presents the mass-normalized currents for ORR from which it is clear that mass specific activity of $Co_3O_4/Co_xCe_{1-x}O_{2-\delta}/C$ is higher than its component oxides at all the considered potentials. This again lays stress on the beneficial synergy that takes place most plausibly due to oxide-oxide interfaces in $Co_3O_4/Co_xCe_{1-x}O_{2-\delta}/C$.

As already mentioned in Section 2.6.9, the ECSAs of the catalysts are assessed from the slopes (double-layer capacitance C_{DL}) of scan-rate dependent CVs in N_2-saturated 0.1 M KOH. These are displayed in Figure 5.11. The equation $ECSA = \frac{C_{DL}}{C_S}$ is used to derive the ECSAs. Cs (the specific capacitance) is taken as 40 $\mu F cm^{-2}$ [23]. The mass-normalized ECSAs are shown in Table 5.3 and is the highest for $Co_3O_4/Co_xCe_{1-x}O_{2-\delta}/C$.

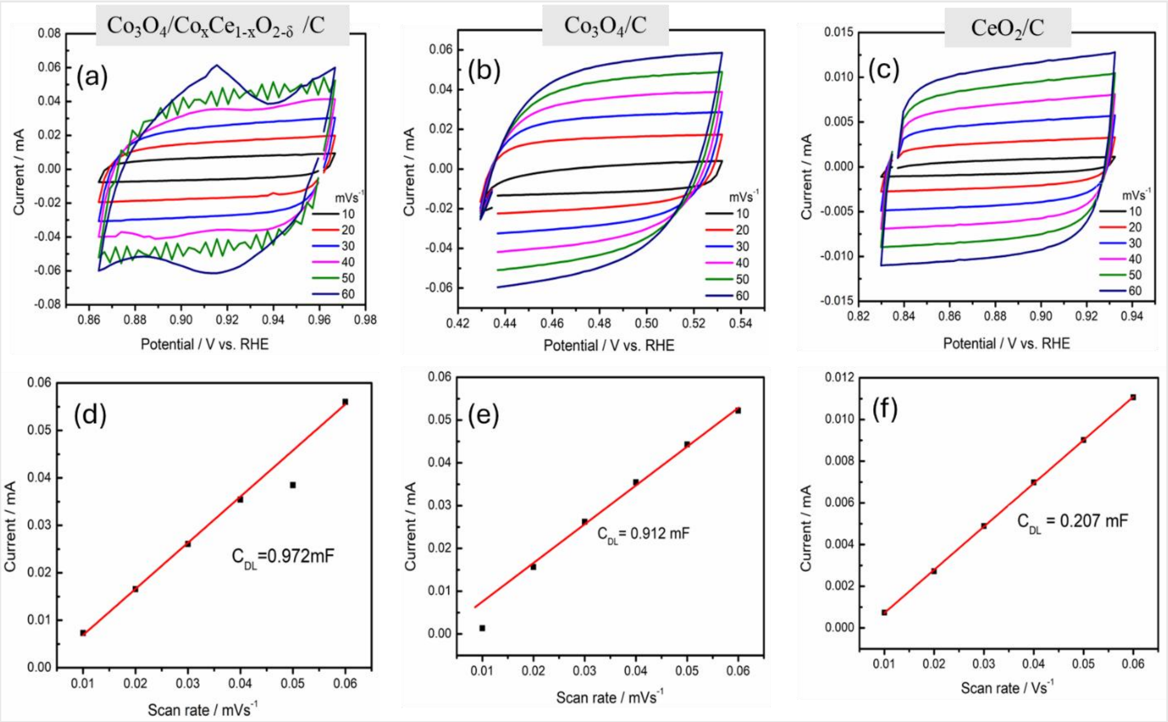

Figure 5.11. (a–c) CVs of the as-synthesized catalysts at different scan rates from 10–60 mV s^{-1}, and (d–e) Double layer capacitance (C_{DL}) derived from slope of charging current of the CVs.

To understand further about the kinetics of the ORR processes for the as-synthesized catalysts, Koutecky-Levich (K-L) analyses are done using the equation mentioned in Section 2.6.6 [24]. The K-L plots at 0.4 V and the number of electrons calculated from the K-L slopes are shown in Figure 5.12. It is found that n~4 for the mix-oxide catalyst $Co_3O_4/Co_xCe_{1-x}O_{2-\delta}/C$ while for its component oxides n<4.

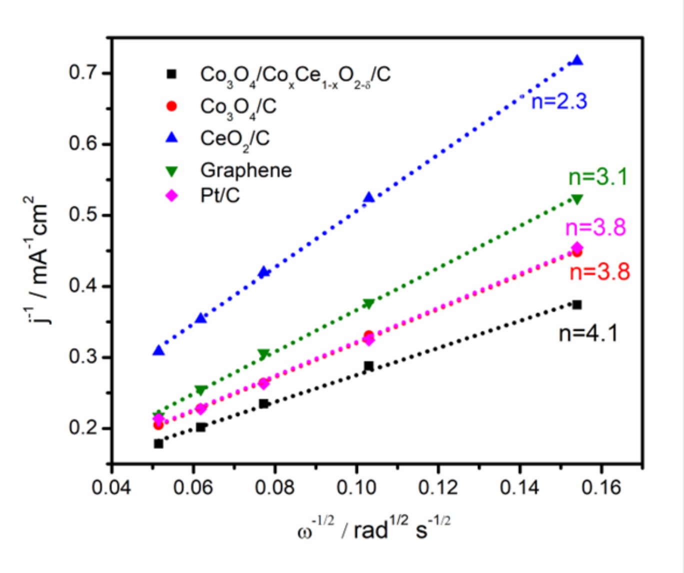

Figure 5.12. K-L plots and derived number of electrons (n) at 0.4 V.

Stability tests viz. ADT and CA are performed to study the chances of practical utility of the as-synthesized catalysts. Owing to the corrosion-prone surface degradation of Pt/C, fast degeneration of Pt/C is inevitable and is a major bottleneck [25]. This is evidenced from the results of ADT shown in Figure 5.13 where Pt/C exhibits an $E_{1/2}$ shift of 6 mV, while there is no observable shift in $E_{1/2}$ for $Co_3O_4/Co_xCe_{1-x}O_{2-\delta}/C$ after 10,000 potential cycles, indicating it to be a promising candidate for practical utility.

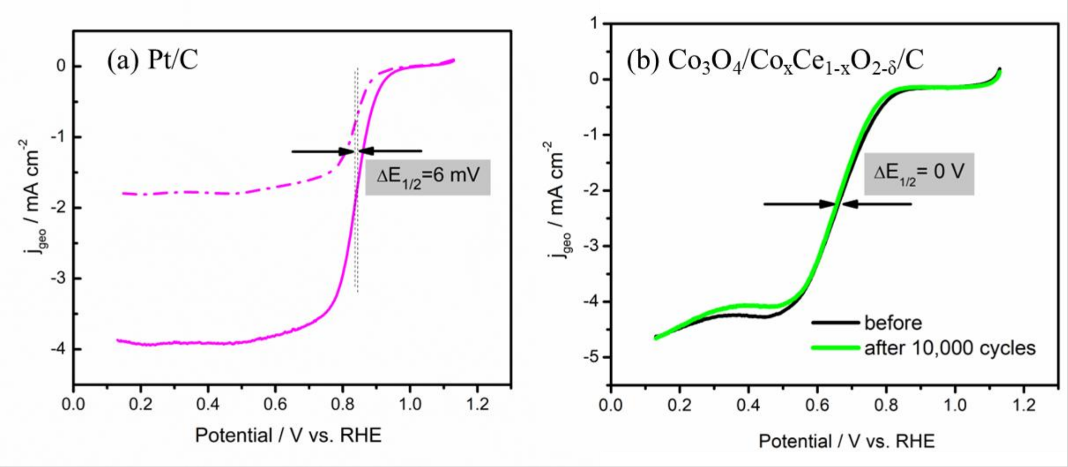

Figure 5.13. LSVs@1600 rpm before and after 10,000 cycles for (a) Pt/C, and (b) $Co_3O_4/Co_xCe_{1-x}O_{2-\delta}/C$ and their Shift of $E_{1/2}$.

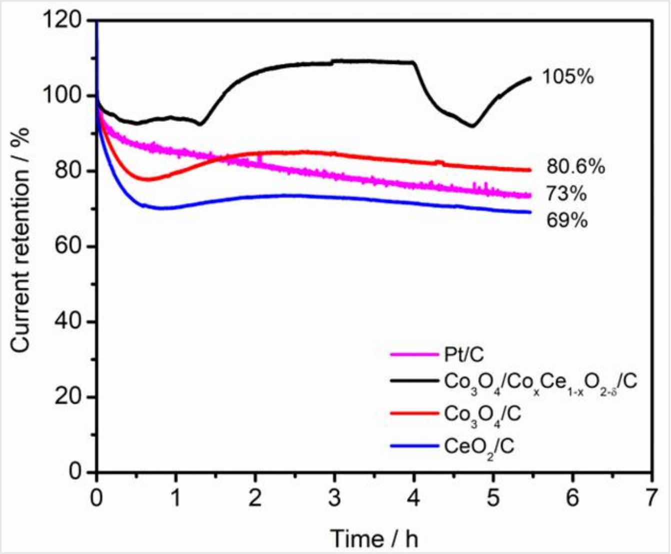

Figure 5.14. Results of 6 h CA test at 0.5 V with their relative current retention.

In a 5.5 h CA test (Figure 5.14) conducted with potential held at 0.5 V, it is observed that $Co_3O_4/Co_xCe_{1-x}O_{2-\delta}/C$ is able to retain higher % of initial current compared to the commercial benchmark Pt/C. It also retains higher current compared to the other two catalysts viz. Co_3O_4/C and CeO_2/C. This highlights that close contact of Co_3O_4 and $Co_xCe_{1-x}O_{2-\delta}/C$ brings upon enhanced stability to the hybrid catalyst of these two oxide moieties. It is to be noted that $Co_3O_4/Co_xCe_{1-x}O_{2-\delta}/C$ has 105% current retention in CA which appeared absurd at first glance. However, the same observation was observed on every repeat of the experiment. Upon a thorough literature survey, we come to understand that the most plausible reason for this is due to surface reconstruction [26–28]. The surface first undergoes some reconstruction and current decreases until the first 1h, after which it starts increasing for another 30 min. Finally, after 1.5 h, it starts decreasing continuously.

The activity of the as-synthesized catalysts towards OER have been tested and the results are as presented in Figure 5.15. Figure 5.15 (a) shows their geometric current densities (j_{geo}) against applied potentials in RDE-LSV at 1600 rpm. The current density of 10 mA cm^{-2} (j_{10}) is marked. The overpotentials calculated from the equation:

$$\eta\ /\mathrm{V} = \mathrm{E(j10)} - 1.23$$

(as mentioned in Section 2.6.10 where E(j10) is the potential to reach 10 mA cm^{-2} for OER) are presented in a bar diagram in Figure 5.15 (b). The hybrid catalyst $Co_3O_4/Co_xCe_{1-x}O_{2-\delta}/C$ exhibits the lowest overpotential of 0.5 V which is equal to the commercial benchmark catalyst RuO_2. Hence, we can say that the hybrid catalyst is a better bifunctional catalyst toward ORR and OER than its component oxides Co_3O_4/C and $Co_3O_4/Co_xCe_{1-x}O_{2-\delta}/C$. The bifunctionality index of $Co_3O_4/Co_xCe_{1-x}O_{2-\delta}/C$ toward ORR and OER is found to be $\Delta E=1.05$ V (Figure 5.15 (c)). It is calculated from equation, $\Delta E\ /V = E(j10) - E_{1/2}$ as explained in Section mentioned in 2.6.10. [29]

The turnover frequencies of the catalysts for OER are calculated as per equation

$$\mathrm{TOF} = \frac{\mathrm{J_g} \times \mathrm{S_{geo}}}{4 \times \mathrm{F} \times \mathrm{n}}$$

where J_g is the current density at an overpotential of 500 mV, S_{geo} is the geometric area of the WE (0.0706 cm^{-2}), F is the Faraday constant (96485 C mol^{-1}) and n is the mole number of the catalyst. TOF is the number of O_2 molecules generated per second per active site and is a direct measure of OER efficiency [1]. The evaluated values are presented in Table 5.3.

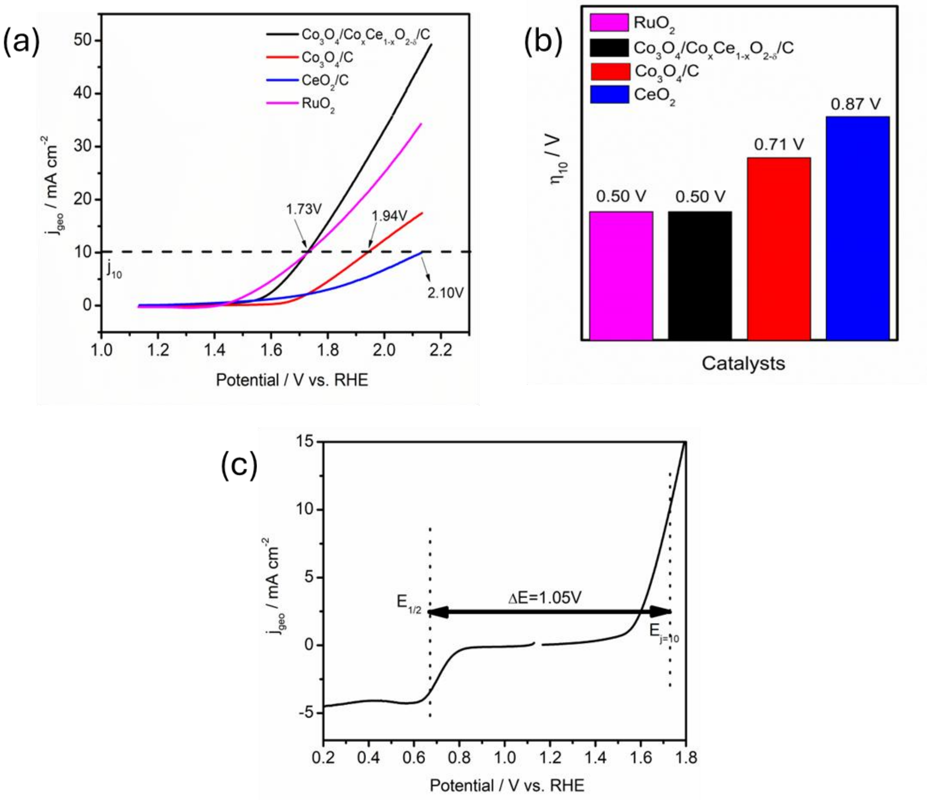

Figure 5.15. (a) LSV@1600 rpm towards OER along with RuO_2, (b) Bar diagram showing the overpotential@10 mA cm^{-2}, and (c) Diagram showing bifunctionality index of $Co_3O_4/Co_xCe_{1-x}O_{2-\delta}/C$ towards ORR and OER.

The TOF is the highest for $Co_3O_4/Co_xCe_{1-x}O_{2-\delta}/C$ (0.259), followed by Co_3O_4/C (0.032) and then by CeO_2/C (0.023). Hence, we see that the overall catalytic performance of the hybrid $Co_3O_4/Co_xCe_{1-x}O_{2-\delta}/C$ is superior to its individual oxides Co_3O_4/C and CeO_2/C. A comparison of all material characteristics reveals that the predominant factor behind this could be the greater amount of oxygen vacancies in $Co_3O_4/Co_xCe_{1-x}O_{2-\delta}/C$. This assumption corroborates well with the higher amount of divalent cobalt ions compared to trivalent ions in $Co_3O_4/Co_xCe_{1-x}O_{2-\delta}/C$. In the previous chapter, some difficulty was faced to correlate the lesser amount of divalent cobalt ions to the greater degree of oxygen vacancy in the mix hybrid $Co_3O_4/CeO_2/C$. In the present chapter, the calcination step has been helpful in removing unwanted hydroxides and/or carbonates apart from doping of Co into CeO_2 and developing beneficial crystalline-amorphous phases in $Co_3O_4/Co_xCe_{1-x}O_{2-\delta}/C$. The findings of this chapter also serves as a double-confirmation for the inferences of the previous chapter.

5.2 Conclusions

In summary, the synthesis of graphene supported CeO_2, Co_3O_4 and $Co_3O_4/Co_xCe_{1-x}O_{2-\delta}$ is demonstrated. The facile charge transfer between Co_3O_4 and $Co_xCe_{1-x}O_{2-\delta}$ promotes higher current generation in the composite $Co_3O_4/Co_xCe_{1-x}O_{2-\delta}$. The co-ordination and interlinkage of Co_3O_4 crystallites with those of $Co_xCe_{1-x}O_{2-\delta}$ offer physico-chemical modifications into the composite, thereby rendering enhanced ORR/OER. Oxygen vacancies lead to low oxidation states of Cobalt. When there are more oxygen vacancies at the surface, the incoming O_2 molecule is automatically shifted to bond with the vacancies and weakens the O−O bond, thereby reducing the chances of H_2O_2 formation. This affinity of O_2 toward vacancies in turn serves to aid in chemical disproportionation of any peroxide formed in the process. The higher degree of oxygen defects in the composite creates a synergistic mechanism which renders it bifunctional, displaying a remarkably lower overpotential towards OER. The fact that it outperforms Pt/C in terms of stability and exhibit very minimal $E_{1/2}$ shift makes it a promising candidate for practical uses in metal-air batteries (MABs) and fuel cells. Although the mechanism is not clear, it is confirmed that a strong beneficial synergy happens when the two components Co_3O_4 and $Co_xCe_{1-x}O_{2-\delta}$ are mixed. This work is yet another testament to the ideology that ceria could intricately enhance the electrochemistry of ORR/OER active transition-metal based catalyst Co_3O_4 and paves the path to explore similar Co-doped ceria and other non-PGM metal oxides/ hydroxides/sulfides towards various other electrochemical reactions to achieve sustainable energy production.

References

[1] Ghosh, D., Manikanta Kumar, M., Retna Raj, C., and Pradhan, D. Bifunctional catalytic activity of solvothermally synthesized CeO_2 nanosphere/NiO nanoflake nanocomposites. *ACS Applied Energy Materials*, 5(5):5666–5679, 2022.

[2] Wang, J., Xiao, X., Liu, Y., Pan, K., Pang, H., and Wei, S. The application of CeO_2-based materials in electrocatalysis. *Journal of Materials Chemistry A*, 7(30):17675–17702, 2019.

[3] Duan, Q., and Chen, H. Synthesis and electrochemical properties of Co_3O_4 nanoparticles by hydrothermal method at different temperatures. *IOP Conference Series: Materials Science and Engineering*, 207:1–8, 2017.

[4] Kashinath, L., and Byrappa, K. Ceria boosting on in situ nitrogen-doped graphene oxide for efficient bifunctional ORR/OER activity. *Frontiers in Chemistry*, 10:1–12, 2022.

[5] Zhong, H., Alberto Estudillo-Wong, L., Gao, Y., Feng, Y., and Alonso-Vante, N. Oxygen vacancies engineering by coordinating oxygen-buffering CeO_2 with CoO_x nanorods as efficient bifunctional oxygen electrode electrocatalyst. *Journal of Energy Chemistry*, 59:615–625, 2021.

[6] Raccichini, R., Varzi, A., Passerini, S., and Scrosati, B. The role of graphene for electrochemical energy storage. *Nature Materials*, 14(3):271–279, 2015.

[7] Polychronopoulou, K., Alkhoori, A. A., Efstathiou, A. M., Jaoude, M. A., Damaskinos, C. M., Baker, M. A., Almutawa, A., Anjum, D. H., Vasiliades, M. A., Belabbes, A., Vega, L. F., Zedan, A. F., and Hinder, S. J. Design aspects of doped CeO_2 for low-temperature catalytic CO oxidation: transient kinetics and DFT approach. *ACS Applied Materials & Interfaces*, 13(19):22391–22415, 2021.

[8] Barnes, P., Jacques, S., and Vickers, M. *Crystallite size and strain*. Retrieved on 1st October 2024 from http://pd.chem.ucl.ac.uk/pdnn/peaks/size.htm,1997.

[9] Wang, Y., Wei, X., Hu, X., Zhou, W., and Zhao, Y. Effect of formic acid treatment on the structure and catalytic activity of Co_3O_4 for N_2O decomposition. *Catalysis Letters*, 149(4):1026–1036, 2019.

[10] Goswami, C., Hazarika, K. K., Yamada, Y., and Bharali, P. Nonprecious hybrid metal oxide for bifunctional oxygen electrodes: endorsing the role of interfaces in electrocatalytic enhancement. *Energy & Fuels*, 35(16):13370–13381, 2021.

[11] Naebe, M., Wang, J., Amini, A., Khayyam, H., Hameed, N., Li, L. H., Chen, Y., and Fox, B. Mechanical property and structure of covalent functionalized graphene/epoxy nanocomposites. *Scientific Reports*, 4:1–7, 2014.

[12] Smyrnioti, M., and Ioannides, T. Synthesis of cobalt-based nanomaterials from organic precursors. In. Maaz, K., editor, *Cobalt*, pages 49–69, ISBN:978-953-51-3667-5. IntechOpen, Croatia, 2017.

[13] Patel, J., and Kiani, A. Comparative study of tribological behaviours of different base greases enhanced by graphene nano platelets. In: *Proceedings of the 3rd International Conference on Theoretical and Applied Nanoscience and Nanotechnology (TANN'19)*, pages 1–4, Ottawa, Canada, 2019.

[14] V G Hadjiev, M. N. I. and I. V. V. The Raman spectra of Co_3O_4. *Journal of Physics C: Solid State Physics*, 21:199–201, 1988.

[15] Su, Z., Yang, W., Wang, C., Xiong, S., Cao, X., Peng, Y., Si, W., Weng, Y., Xue, M., and Li, J. Roles of oxygen vacancies in the bulk and surface of CeO_2 for Toluene Catalytic Combustion. *Environmental Science & Technology*, 54(19):12684–12692, 2020.

[16] Goswami, C., Yamada, Y., Matus, E. V., Ismagilov, I. Z., Kerzhentsev, M., and Bharali, P. Elucidating the role of oxide-oxide/carbon interfaces of CuO_x-CeO_2/C in boosting electrocatalytic performance. *Langmuir*, 36(49):15141–15152, 2020.

[17] Maslakov, K. I., Teterin, Y. A., Ryzhkov, M. V., Popel, A. J., Teterin, A. Y., Ivanov, K. E., Kalmykov, S. N., Petrov, V. G., Petrov, P. K., and Farnan, I. The electronic structure and the nature of the chemical bond in CeO_2. *Physical Chemistry Chemical Physics*, 20(23):16167–16175, 2018.

[18] Huang, J., Borca, C. N., Huthwelker, T., Yüzbasi, N. S., Baster, D., El Kazzi, M., Schneider, C. W., Schmidt, T. J., and Fabbri, E. Surface oxidation/spin state determines oxygen evolution reaction activity of cobalt-based catalysts in acidic environment. *Nature Communications*, 15(1):1–9, 2024.

[19] Chelliah, P., Wabaidur, S. M., Sharma, H. P., and Jweeg, M. J. Green synthesis and characterizations of cobalt oxide. *Water*, 15(5):1–16, 2023.

[20] Li, L., Yuan, Q., Ye, S., Fu, Y., Ren, X., Zhang, Q., and Liu, J. In situ formed lithium ionic conductor thin film on the surface of high-crystal-layered $LiCoO_2$ as a high-voltage cathode material. *Materials Chemistry Frontiers*, 5(16):6171–6181, 2021.

[21] Li, X., Zhao, Z. J., Zeng, L., Zhao, J., Tian, H., Chen, S., Li, K., Sang, S., and Gong, J. On the role of Ce in CO_2 adsorption and activation over lanthanum species. *Chemical Science*, 9(14):3426–3437, 2018.

[22] Seo, J., Gowda, A., and Babu, S. V. Almost complete removal of ceria particles down to 10 nm size from silicon dioxide surfaces. *ECS Journal of Solid State Science and Technology*, 7(5):243–252, 2018.

[23] Chutia, B., Patowary, S., Misra, A., Rao, K. N., and Bharali, P. Morphology effect of Co_3O_4 nanooctahedron in boosting oxygen reduction and oxygen evolution reactions. *Energy & Fuels*, 36:13863–13872, 2022.

[24] Chetry, R., Chutia, B., Patowary, S., Borah, B. J., Sudarsanam, P., and Bharali, P. Electronic modulation of Pd/C by simultaneous doping of Cu and Co tendering a highly durable and methanol-tolerant oxygen reduction electrocatalyst. *Energy & Fuels*, 37(13):9557–9567, 2023.

[25] Luo, Y., Wu, Y., Li, B., Mo, T., Li, Y., Feng, S. P., Qu, J., and Chu, P. K. Development and application of fuel cells in the automobile industry. *Journal of Energy Storage*, 42:1–19, 2021.

[26] Chen, J., Zhou, N., Wang, H., Peng, Z., Li, H., Tang, Y., and Liu, K. Synergistically enhanced oxygen reduction activity of MnO_x-CeO_2/Ketjenblack composites. *Chemical Communications*, 51(50):10123–10126, 2015.

[27] Mokdad, S., Boukazoula, A., Chouchane, K., Saib, F., Trari, M., and Abdi, A. Electrocatalytic activity of electrodeposited CoO_x thin film on low-carbon unalloyed steel substrate toward electrochemical oxygen evolution reaction (OER). *Chemical Papers*, 77(9):4979–4992, 2023.

[28] Karmakar, A., Karthick, K., Sankar, S. S., Kumaravel, S., Ragunath, M., and Kundu, S. Oxygen vacancy enriched $NiMoO_4$ nanorods via microwave heating: a promising highly stable electrocatalyst for total water splitting. *Journal of Materials Chemistry A*, 9(19):11691–11704, 2021.

[29] Goswami, C. Design of platinum-free nano-electrocatalysts for fuel cell reactions. PhD thesis, Department of Chemical Sciences, Tezpur University, Assam, India, 2021.